A genome-wide nucleosome-resolution map of promoter-centered interactions in human cells corroborates the enhancer-promoter looping model

Arkadiy K. Golov[1,2], Alexey A. Gavrilov[1], Noam Kaplan[2]*, Sergey V. Razin[1,3]*

[1]Institute of Gene Biology, Russian Academy of Sciences, Moscow, Russia
[2]Department of Physiology, Biophysics & Systems Biology, Rappaport Faculty of Medicine, Technion - Israel Institute of Technology, Haifa, Israel
[3]Faculty of Biology, Lomonosov Moscow State University, Moscow, Russia

*Corresponding author

Abstract

The enhancer-promoter looping model, in which enhancers activate their target genes via physical contact, has long dominated the field of gene regulation. However, the ubiquity of this model has been questioned due to evidence of alternative mechanisms and the lack of its systematic validation, primarily owing to the absence of suitable experimental techniques. In this study, we present a new MNase-based proximity ligation method called MChIP-C, allowing for the measurement of protein-mediated chromatin interactions at single-nucleosome resolution on a genome-wide scale. By applying MChIP-C to study H3K4me3 promoter-centered interactions in K562 cells, we found that it had greatly improved resolution and sensitivity compared to restriction endonuclease-based C-methods. This allowed us to identify EP300 histone acetyltransferase and the SWI/SNF remodeling complex as potential candidates for establishing and/or maintaining enhancer-promoter interactions. Finally, leveraging data from published CRISPRi screens, we found that most functionally-verified enhancers do physically interact with their cognate promoters, supporting the enhancer-promoter looping model.

Introduction

For decades since the discovery of the first enhancers, the enhancer-promoter (E-P) looping model, in which enhancers activate their target genes via physical contact, has dominated the field[1,2]. However, direct empirical evidence for this hypothesis has been scarce, and only a handful of credible enhancers were demonstrated to be in physical contact with their promoter partners. These include classical enhancers and their established targets such as globin genes, HoxD cluster genes, Shh and PAX6 genes[3–9]. Simultaneously, recent microscopy observations do not seem to align well with the E-P looping model[10,11].

The development of genomic assays based on proximity-ligation of chromatin, commonly known as C-methods[12–14], has revolutionized the study of genome spatial organization, providing a complementary view to microscopic approaches[14–16]. Both the resolution and throughput of genome-wide C-methods were instrumental in defining salient structural features of mammalian chromatin, including genomic compartments, topologically associating domains (TADs) and cohesin-dependent CTCF point interactions[17–22]. However, unlike CTCF-based interactions, very few specific E-P interactions were observed with conventional restriction enzyme-based C-methods. Initially, sequencing depth inherently limited the resolution of all vs all approaches such as Hi-C, and thus a number of targeted approaches were developed. In-solution hybridization (CaptureC, CaptureHi-C) or immunoprecipitation (ChIA-PET, HiChIP, PLAC-seq) are exploited in these methods to enrich for interactions of specific regions of interest, thus decreasing the sequencing burden and allowing higher resolution[23–27]. While targeted methods clearly revealed a statistical preference of promoters to be in spatial proximity to enhancer-like regions and enabled detection of some individual E-P

interactions, in some cases functionally-verified enhancers did not show spatial proximity to the promoters of their targets as measured with C-methods[10,28], raising further questions concerning the universality and functional relevance of E-P looping.

Although targeted methods have circumvented sequencing-depth limitations, the resolution of C-methods based on restriction endonuclease digestion cannot overcome the inherent restriction fragment length limitation, which often results in a high level of background noise and the inability to distinguish CTCF-based interactions from other types of chromatin spatial interactions[29]. The introduction of MNase-based C-methods, such as Micro-C and its targeted oligonucleotide hybridization-based counterpart MCC, reduced the resolution limitation, allowing finer chromatin structures to be distinguished[6,30,31]. Crucially, the usage of MNase also allowed milder detergent pretreatment of crosslinked cells, increasing the sensitivity of Micro-C, MCC and related techniques by retaining E-P interactions, which appear to be more susceptible to experimental conditions than CTCF-based chromatin interactions[32–34]. In parallel, the development of genomic and epigenomic CRISPR-based functional screens have greatly expanded the amount of available data on functional E-P interactions. Taken together, these advancements now open the door for the systematic investigation of the spatiotemporal mechanisms underlying distal control of mammalian transcription.

Here we present a new MNase-based C-method, MChIP-C, which allows measuring promoter-centered interactions at single nucleosome resolution on a genome-wide scale. We applied MChIP-C to construct a nucleosome-resolution map of promoter-centered interactions in human K562 cells. Taking advantage of the significantly improved resolution and sensitivity of our approach compared to restriction endonuclease-based C-methods, we investigated the molecular underpinnings of promoter-centered chromatin spatial interactions and identified EP300 histone acetyltransferase and the SWI/SNF remodeling complex as candidates for establishing and/or maintaining E-P spatial contacts. Finally, by comparing our chromatin interaction data with previously published results of CRISPRi screens[35,36], we found that most functionally verified enhancers do physically interact with their cognate promoters, supporting the E-P looping model of enhancer activity and implying that in general physical interactions are central to enhancer activity in mammalian cells.

Results

MChIP-C: antibody-based targeted measurement of genome architecture at single-nucleosome resolution

We developed MChIP-C, a novel MNase-based proximity ligation technique which combines the genome-wide throughput of HiChIP with the exceptional resolution and sensitivity of MCC (Fig. 1a). The protocol starts similar to MCC, where cells are crosslinked with formaldehyde and permeabilized with digitonin. This milder cell permeabilization procedure has been shown to provide higher sensitivity for detecting E-P interactions[6]. Next, chromatin is digested with micrococcal nuclease, DNA ends are blunted and proximity ligated. This is followed by sonication and chromatin immunoprecipitation with a specific antibody, as in HiChIP or PLAC-seq (Fig. 1a). Crosslinks are then reversed, and DNA is purified, followed by library preparation and sequencing. As in MCC, we avoided using biotin to enrich for ligated fragments, potentially increasing library complexity, but also resulting in a low proportion of informative chimeric read pairs in the sequencing libraries. To partially mitigate this, we decreased the level of DNA fragmentation and selected for longer DNA fragments (see Methods).

We performed 4 biological replicates of MChIP-C experiment on K562 cells using anti-H3K4me3 antibodies to focus on spatial interactions of active promoters. The MChIP-C libraries were paired-end sequenced with a total of ~3.5B read pairs, yielding ~3B uniquely mapped reads (Fig. 1b, Fig. S1b, Supplementary Table S2). ~91.5% (~2.77B) of these mapped within 1 kb of each other and ~4% (~120M) mapped further than 5 kb away from each other. While the 4% fraction of informative

reads was low relative to restriction enzyme-based C-methods (e.g. >60% informative reads in PLAC-seq), it is comparable to MCC (0.5-5% informative reads, see Methods).
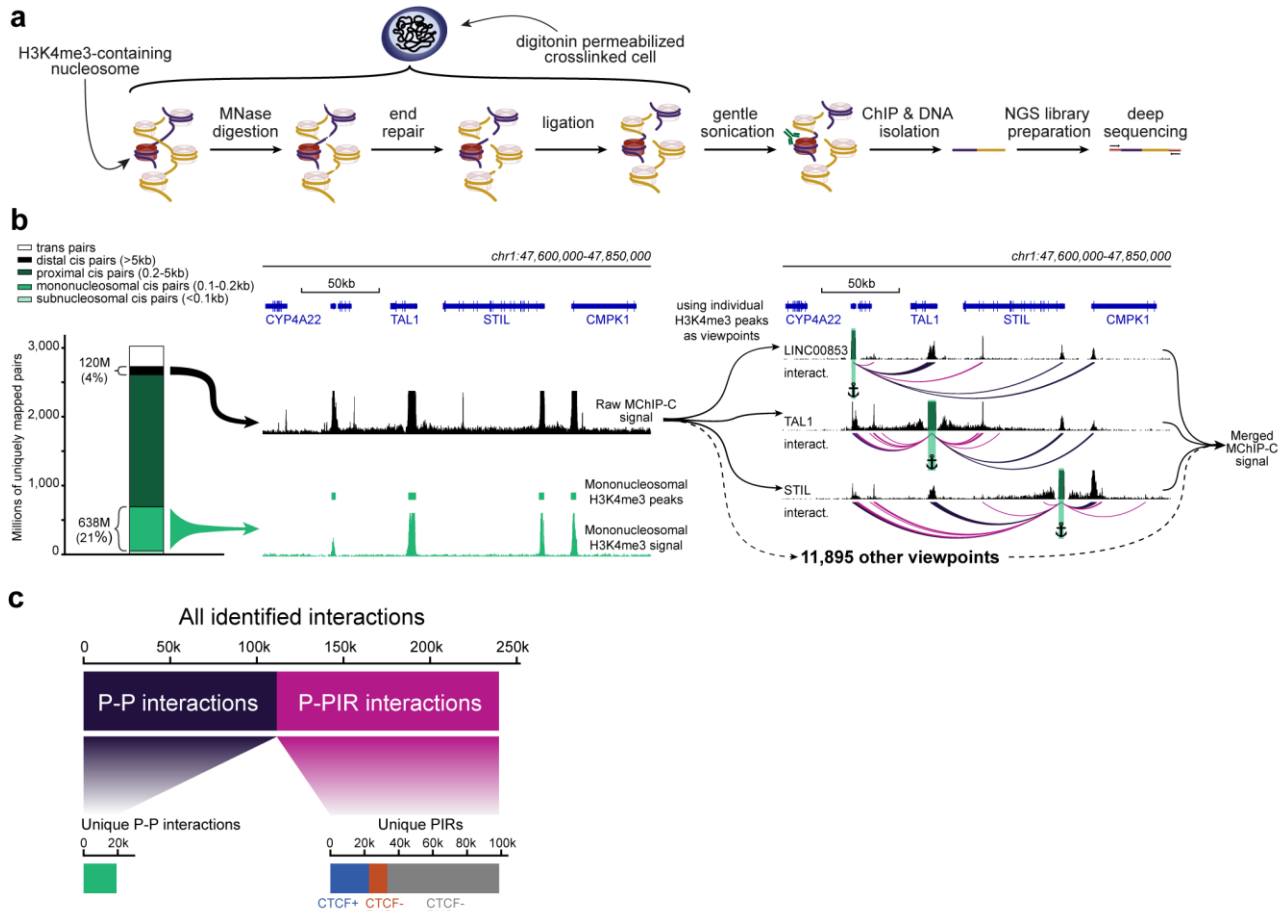

Figure 1. MChIP-C experimental and computational workflow. a. An overview of the MChIP-C experimental procedure. **b.** General MChIP-C analysis pipeline. A 250-kb genomic region surrounding the TAL1 gene is shown with H3K4me3 MChIP-C profiles in K562 cells. Positions of individual viewpoints are highlighted by green rectangles and anchors. Identified MChIP-C interactions are shown as magenta (P-PIR) and dark violet (P-P) arcs. **c.** Summary statistics for all 239,779 promoter-centered MChIP-C interactions identified in K562 cells.

After read mapping, we identified active promoters by first selecting nucleosome-size convergently mapping read pairs to obtain H3K4me3 occupancy profiles. We found that the profiles of replicates were highly similar (Pearson correlation 0.95-0.97) and match standard H3K4me3 ChIP-seq (Pearson correlation 0.89-0.91) (Fig. S1c,d). Next, we identified 11,898 consensus peaks amongst replicates and found these mostly colocalized with active RNA polymerase II TSSs (Fig. S1e, Supplementary Table S3).

We then proceeded to map promoter interactions. We defined the H3K4me3 peaks as interaction viewpoints and selected the reads mapping to each of these viewpoints, resulting in 11,898 4C-like viewpoint interaction profiles. To gain a general overview of the data, we summed the profiles of all viewpoints into a single genome-wide profile which we refer to as "merged MChIP-C" (Fig. 1b). Both viewpoint-specific and merged MChIP-C correlated well between replicates (Pearson correlation 0.83-0.93 for merged profiles and 0.64-0.76 for viewpoint-separated profiles) (Fig. S1f), and therefore we combined all replicates, resulting in single-nucleosome resolution interaction profiles for 10,949 active promoters, after filtering low-coverage viewpoints.

The obtained interaction profiles demonstrate that promoters interact with each other and with non-promoter regions (Fig. 1b). We systematically identified localized interactions by searching for 250 bp bins with significantly higher than expected MChIP-C signal. Overall, we detected 111,543 promoter-promoter bin (P-P) interactions and 128,236 promoter-nonpromoter bin interactions (Fig.

1c, Supplementary Table S4). Both types of interactions were mostly localized within TADs (Fig. S1h). We excluded P-P interactions from subsequent analyses and focused on 128,236 promoter-nonpromoter interactions linking 10,707 viewpoints with 98,721 unique nonpromoter bins (Supplementary Table S5) which we refer to as PIRs (Promoter Interacting Regions).

MChIP-C provides a sensitive genome-wide view of promoter-centered interactions

We then asked how MChIP-C compares to similar approaches based on standard restriction enzymes. HiChIP and PLAC-seq are directly comparable to MChIP-C, as both HiChIP and PLAC-seq combine Hi-C with chromatin immunoprecipitation. Specifically, we compared our data to those of Chen et al.[37], who used PLAC-seq with anti-H3K4me3 antibodies in K562 cells. We first visually compared the PLAC-seq and MChIP-C proximity ligation profiles of a number of genes with well-described regulatory landscape in K562 cells: MYC, GATA1 and HBG2. We found that MChIP-C profiles showed clear highly-localized interaction peaks corresponding to the CTCF-bound sites and enhancers known to control the expression of these genes (Fig. 2a, Fig. S2). For instance, the MYC gene has seven well-characterized K562-specific enhancer elements (e1-e7) spread along the 2 Mb region downstream of the gene[33,38] and MChIPC allowed detection of interactions between MYC promoter and 5 of these sites. PLAC-seq profiles are by contrast much noisier and virtually devoid of any clear peaks corresponding to either CTCF sites or known enhancers of the interrogated genes.
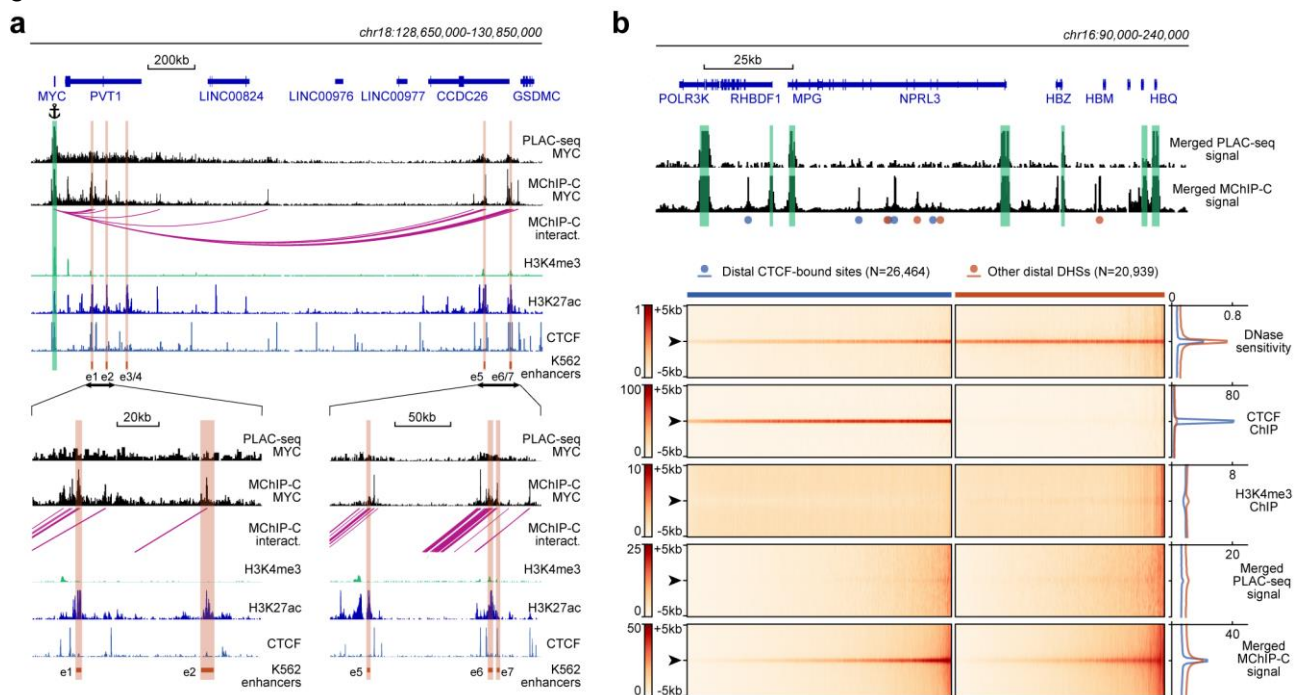

Figure 2. Comparison of MChIP-C with PLAC-seq. a. Top: MChIP-C and PLAC-seq interaction profiles of the MYC promoter in K562 cells. MChIP-C interactions of the MYC promoter are shown as magenta arcs. Positions of 7 (e1-e7) CRISPRi-verified K562 MYC enhancers are highlighted as orange rectangles. Bottom: zoom in on two enhancer clusters. **b.** Systematic comparison of merged MChIP-C and merged PLAC-seq signals in distal regulatory sites. Top: Merged MChIP-C and merged PLAC-seq profiles in a 150-kb genomic region surrounding the α-globin gene domain. Viewpoints are highlighted as green rectangles. Positions of CTCF-bound and CTCF-less DNase hypersensitive sites outside viewpoints are depicted as blue and orange circles. Bottom: Heatmaps and averaged profiles of DNase sensitivity, CTCF ChIP, H3K4me3 ChIP, merged MChIP-C and merged PLAC-seq signals centered on distal CTCF-bound and CTCF-less DNase hypersensitive sites.

Next, we compared MChIP-C and PLAC-seq in a more systematic way by examining their merged interaction profiles around promoter-distal DHSs (Fig.2b). We observed that in MChIP-C 22.9% of PIRs colocalize with CTCF-bound sites (Fig. 1c, Supplementary Table S5). We separately examined DHSs with and without CTCF, and found that both types of DHSs show increased interaction signal relative to background. In contrast, we found that PLAC-seq shows a very weak enrichment of interactions at DHSs, even for those bound by CTCF. Thus, in line with other recent reports on MNase-based C-methods[6,30,31,39–41], our results suggest that MChIP-C achieves superior sensitivity and resolution compared to C-methods based on standard restriction enzymes.

CTCF orientation-biased interaction of CTCF-bound sites and promoters

As we observed abundance of CTCF-bound PIRs in MChIP-C data, we asked whether these CTCF-promoter interactions correspond to loop extrusion-driven loops between convergent CTCF sites easily noticeable on the Hi-C heatmaps[21,42–44]. About half of the identified promoter-CTCF interactions (21,152 out of 41,230) showed CTCF binding at the promoter side as well. Interestingly, only 568 (~2.7%) of those directly correspond to CTCF-CTCF loops reported in a previous Hi-C study[21]. The other half of the MChIP-C interactions containing a CTCF-bound PIR (20,078/41,230) do not show CTCF binding at the promoter side at all. For this set of CTCF-less promoters, we analyzed the orientation of CTCF motifs in PIRs relative to the position of the promoter. We found that promoters preferentially interact with CTCF-bound sites if CTCF motifs are oriented towards the promoter (79% towards vs 21% away) (Fig. 3a). This bias holds true regardless of the position of the CTCF site relative to the transcription direction (80% vs 20% for upstream CTCF sites and 79% vs 21% for downstream sites). We also observed this bias if both the promoter and the PIR have CTCF ChIP-seq signal, but CTCF motifs are not in convergent/divergent orientation (Fig. S3). We conclude that interactions of promoters with CTCF-bound sites are biased by CTCF orientation, regardless of CTCF binding at the promoter side. This orientation bias suggests the possible involvement of loop extrusion.

Promoter-interacting enhancers bind a distinct and diverse set of protein factors

We next asked whether the sensitivity and resolution of MChIP-C could allow us to examine the molecular underpinnings of promoter-centered interactions which are not CTCF-based. While the question of what factors underlie P-E interactions is fundamental, this type of analysis would be problematic with restriction enzyme-based C-methods due to their inability to precisely map loop anchors to protein binding sites. To determine protein factors associated with PIRs, we first overlaid MChIP-C PIRs with 271 ChIP-seq profiles for K562 cells (Supplementary Table S1). Most of the analyzed transcription-related factors and histone post-translational modifications are substantially enriched in MChIP-C PIRs (4-25X) (Fig. 3b, Supplementary Table S6). Notable exceptions are facultative heterochromatin-associated histone mark H3K27me3 (1113 overlaps, 1866 (SD=43) expected by chance) and LINE1-binding protein ZNF146 (184 overlaps, 174 (SD=12) expected by chance). As expected, CTCF (22,448 / 1,589 (SD=39)), cohesin subunits RAD21 (10,629 / 398 (SD=17)) and SMC3 (12,838 / 557 (SD=23)) are among the most highly enriched factors.
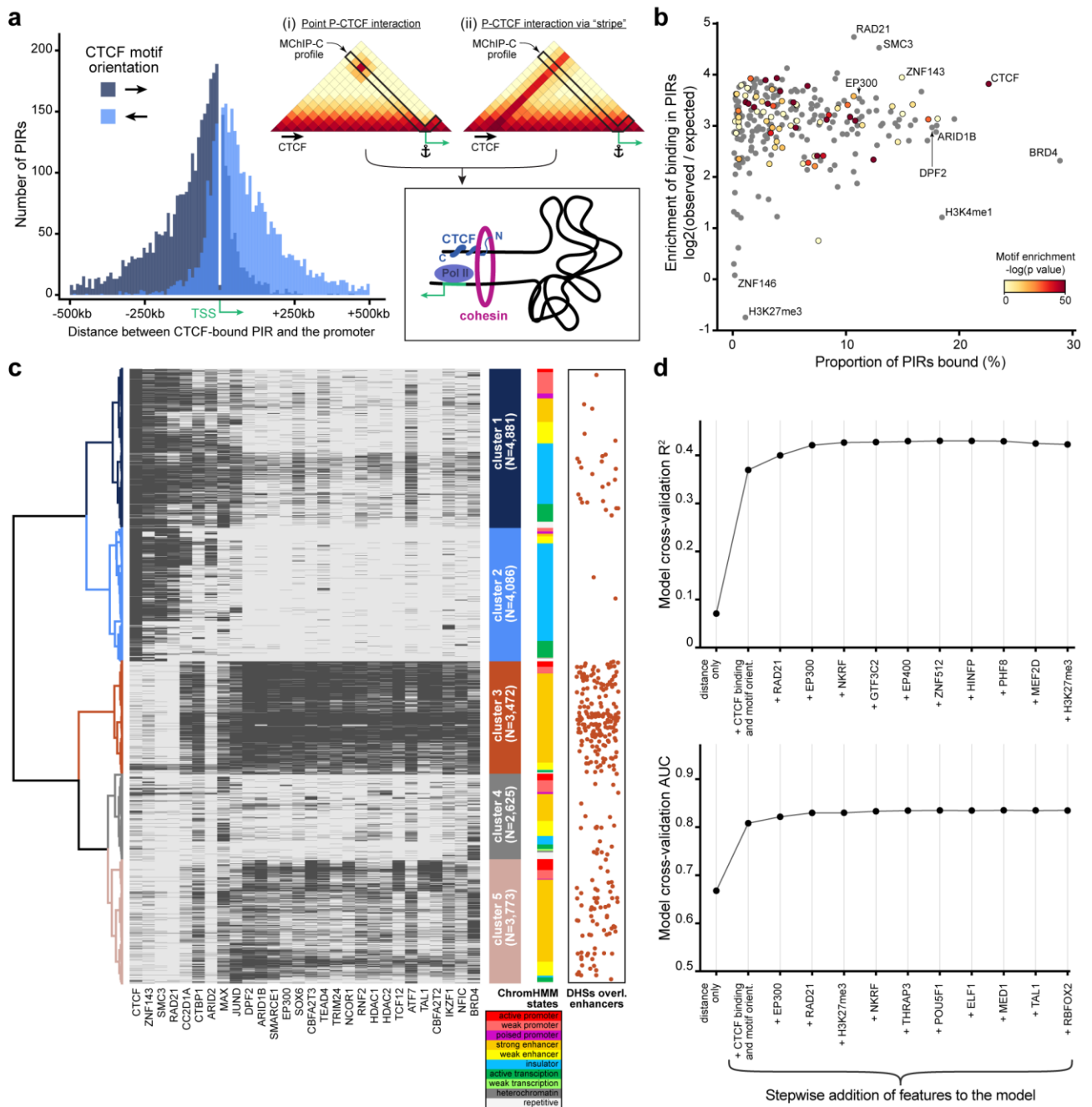
Figure 3. Analysis of protein factors underlying MChIP-C interactions. a. Left: CTCF-motif orientation bias in regions interacting with CTCF-less promoters. The majority (~79%) of CTCF motifs are oriented towards the interacting promoter. Right: Schematic of two hypothetical loop extrusion dependent mechanisms that can account for the observed pattern: promoter LE-barrier activity (i) or CTCF-originating interaction stripes (ii). **b.** Enrichment of transcription-related factor (TRF) binding in MChIP-C PIRs. Y-axis represents enrichment (log2(observed/expected)) of binding for 271 examined TRFs, x-axis – proportion of TRF-bound PIRs, color – enrichment of corresponding motifs in PIRs (grey color is assigned to TRFs lacking DNA-binding motif). **c.** Hierarchical clustering of PIR-overlapping DHSs (N=18,837). The binding status of 168 TRFs highly enriched in PIRs are used as binary features. Binding of 28 selected TRFs (see Methods) in each PIR-overlapping DHS is shown as a heatmap. ChromHMM chromatin state distributions in each cluster are shown. DHSs overlapping CRISPRi-verified K562 enhancers[35,36] are shown as orange dots. **d.** Predictive performance (3-fold cross-validation R2/AUC) of random forest models predicting MChIP-C signal for DHS-promoter pairs. Starting with an initial model based on distance and CTCF, the most predictive TRF features are added incrementally to the model (left to right).

Rather than separately consider each factor associated with a PIR, we next used hierarchical clustering to partition PIR-overlapping DHSs (i.e. promoter interacting DHSs) (N=18,837) into groups according to the factor binding profile of each DHS. We identified 5 major clusters (Fig. 3c, Fig. S4a, Supplementary Table S7). Clusters 1 (N=4,881) and 2 (N=4,086) were almost universally bound by the structural factors CTCF (98.2% and 97.3% in clusters 1 and 2 correspondingly), cohesin subunits SMC3 (87.2% and 73.8%) and RAD21 (70.4% and 60.8%) as well as zinc finger protein ZNF143 (89.5% and 69.5%). A total of 24,633 interactions with a median distance of ~91 kb were anchored in DHSs from these two clusters (Fig. S4b). DHSs from clusters 3 (N=3,472), 4 (N=2,625) and 5 (N=3,773) contained almost no CTCF- or cohesin-bound sites. No factors were overrepresented in cluster 4, while clusters 3 and 5 were enriched in dozens of transcription-related factors. Notably, CRISPRi-confirmed enhancers[35,36] were significantly overrepresented in cluster 3 DHSs (182/293 overlaps; one-sided binomial test, P = 4.85*10^{-61}), and we thus labeled P-cluster 3 DHS interactions as regulatory interactions. Overall, there were 8,037 regulatory interactions, which tended to be shorter (median length ~48kb) than structural ones (Fig. S4b). Interestingly, cohesin subunits were absent in the vast majority of class 3 DHSs. This may suggest that cohesin is not involved in the formation and maintenance of the regulatory interactions, as opposed to what was previously suggested[45,46]. In conclusion, we find diverse types of promoter interacting DHSs associated with the binding of different sets of factors. However, the clustering analysis was not able to pinpoint a specific factor, beyond CTCF and cohesin, which would parsimoniously explain the observed promoter-DHS interactions.

Genomic distance, CTCF, cohesin and EP300 are key determinants of promoter-centered interactions

We next sought to pinpoint additional factors which underlie promoter-centered interactions and to directly test their predictive power. We used a greedy forward feature selection approach, based on a random forest regression model trained to predict the strength of MChIP-C interactions between promoters and DHS sites (N=104,164). The initial random forest model consisted of five features: DHS-promoter genomic distance, CTCF ChIP-seq signal at both the promoter and the DHS, and motif orientations on both the promoter and the DHS. This initial model was able to explain ~37% of variance in the MChIP-C signal. Then, we iteratively added the most predictive feature out of a set of 270 ChIP-seq profiles, where predictivity is calculated as R^2 in 3-fold cross validation. Using this strategy, cohesin subunit RAD21 and histone acetyltransferase EP300 were automatically selected, after which predictive performance plateaued at an R^2 of ~43% (Fig. 3d). We also found the same factors as the most predictive of binary outcomes (high/low MChIP-C signal) reaching an AUC of 0.825.

As CTCF and RAD21 are mostly associated with structural loops, we asked whether EP300 mainly underlies regulatory interactions. Indeed, we find that EP300 was 3-fold enriched in cluster 3 DHSs and 93.5% of cluster 3 DHSs showed EP300 binding. Interestingly, we noticed that the only proteins that had more binding sites in cluster 3 DHSs are subunits of the SWI/SNF remodeling complex: DPF2 (97.5%), ARID1B (95.6%) and SMARCE1 (93.6%) (Fig. 3c). EP300 has been found to directly interact with SWI/SNF-complex[47,48] and their chromatin binding profiles are highly correlated (Pearson correlation 0.65-0.70). Revisiting the binding profiles of these SWI/SNF subunits, we found their predictive power to be very close to that of EP300 (Fig. S4c). We also specifically examined the predictive power of RNA polymerase II, mediator complex, YY1 and BRD4, which were previously suggested to be associated with enhancer-promoter interaction[45,49–51], but found these features to be weaker predictors of MChIP-C signal (Fig. S4c). Thus, we suggest that EP300 and/or the SWI/SNF complex might be involved in the formation of regulatory chromatin interactions independently of CTCF and cohesin.

MChIP-C data are largely consistent with the looping model of enhancer activity

The apparent lack of spatial proximity between experimentally-validated enhancers and their cognate promoters in some studies employing C-methods has raised doubts regarding the classical promoter-enhancer looping model. We thus asked whether the enhanced sensitivity and resolution of MChIP-C could shed light on the fundamental question of whether enhancers should be in spatial proximity to their targets in order to activate them. To address this, we systematically compared MChIP-C profiles with functionally verified E-P pairs identified by CRISPRi screens in K562[35,36]. We compared 351 functionally verified E-P pairs, in which targeting CRISPRi to the enhancer changed the expression of the target, with 53,660 putative non-regulatory DHS-P pairs, in which CRISPRi showed no effect. Notably, we found that 61.5% (216/351, 95% CI [56.2%; 66.6%]) of the verified pairs have underlying spatial interactions detected with MChIP-C, while only 6.3% (3,399/53,660, 95% CI [6.1%; 6.5%]) of non-regulatory DHS-P pairs show such interactions (Fig. 4a,b; Supplementary Tables S8 and S9). Thus, we conclude that a majority of experimentally-validated enhancers exhibit interaction with their target promoters.
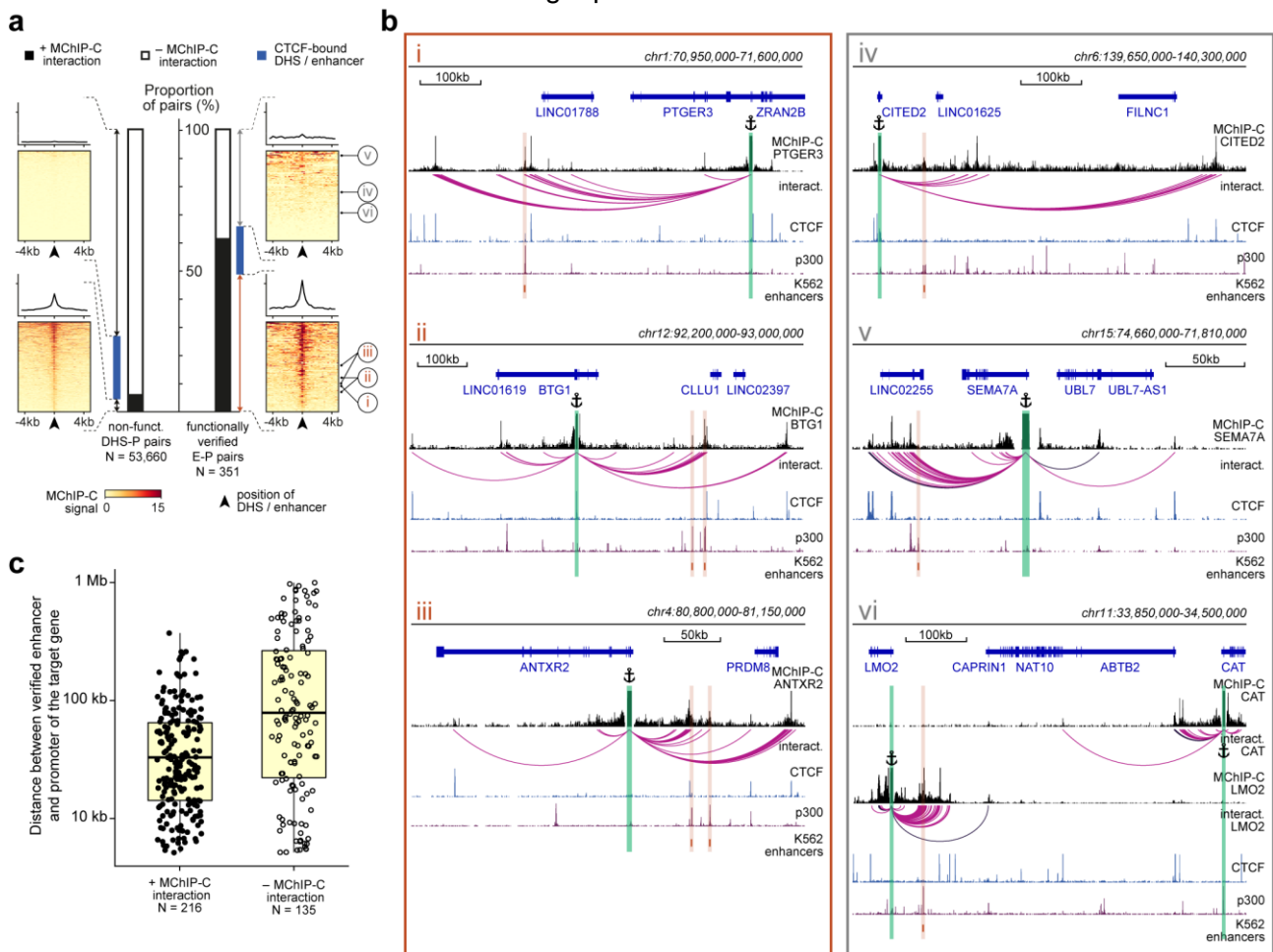

Figure 4. The majority of functionally-verified enhancers do physically interact with their target promoters. a. Bar plots representing the proportion of MChIP-C interacting pairs among nonfunctional DHS-P pairs and CRISPRi-verified E-P pairs. Heatmaps and average profiles of MChIP-C signal are shown for individual subsets. CRISPRi-verified enhancers shown in panel b are indicated by roman numerals. **b.** Examples of MChIP-C profiles for promoters physically interacting with their functionally verified enhancers (MChIP-C interaction has been found) (i-iii) and not interacting with them (MChIP-C interaction has not been found) (iv-vi). The viewpoints are highlighted by anchor symbols and green rectangles, the enhancers are highlighted by orange rectangles. **c.** Distance distribution boxplots for verified E-P pairs with and without MChIP-C interactions.

Next, we inspected more closely cases in which validated E-P pairs did not show interaction in MChIP-C (Fig. 4b, iv-vi). First, we noticed that, in some instances, weak interactions were visually apparent but were missed by the interaction calling algorithm, especially in viewpoints that had low coverage (Fig. 4b, iv). Indeed, when we considered 175/351 validated E-P pairs corresponding to high-coverage viewpoints, 70.3% (123/175, 95% CI [62.8%; 76.8%]) had underlying MChIP-C spatial interactions. Second, in some cases we noticed adjacent (few kbp) H3K27ac-positive regions clearly interacting with the expected promoter, possibly suggesting inexact identification of the enhancer position due to the limited resolution of the CRISPRi screens[36] (Fig. 4b, v). Third, CRISPRi-detected E-P interactions are not guaranteed to represent direct effects. In some cases, an enhancer may impose secondary influence through the action of the directly targeted gene[36]. For example, CRISPRi showed that an enhancer near LMO2 affects both LMO2 and CAT, a gene approximately 400kb away. MChIP-C only shows interaction with LMO2 but not with CAT (Fig. 4b, vi). We hypothesize that regulatory relationships between this enhancer and CAT are mediated through transcription factor encoded by the LMO2 gene and thus it is unreasonable to expect spatial interaction between them. Additionally, we expect that interactions between enhancers and indirect targets would not be overrepresented at short genomic distances. Indeed, we observed that the genomic distance between non-interacting E-P pairs (median 75 kb) is substantially larger than between interacting E-P pairs (median 28 kb), supporting the possibility of indirect activation (Fig. 4c). Another possible source of indirect effects are CTCF-occupied insulators. As was pointed out previously[35], these sites can affect the expression of genes in CRISPRi screens, but do not need to spatially interact with their targets. Indeed, 59 of 351 verified E-P pairs show CTCF occupancy at enhancer side, and 14 of these lack E-P interaction in MChIP-C. In sum, we conclude that the fraction of verified E-P pairs in which we observe a spatial interaction is likely underestimated, which further supports the notion that most enhancers physically interact with their targets and that many such interactions may have not been identified previously due to technical limitations of the employed methods.

Discussion

In this study, we present a new high-resolution genome-wide C-method, MChIP-C, which integrates proximity ligation of MNase-digested chromatin with chromatin immunoprecipitation and deep sequencing. Like other MNase-based C-methods, MChIP-C allows precise mapping of localized chromatin interactions including E-P contacts which often evade capture by endonuclease-based C-methods[29]. Uniquely, MChIP-C combines the resolution and sensitivity of MCC with the genome-wide scale of Micro-C.

Applying H3K4me3-directed MChIP-C to K562 cells, we explored the spatial connectivity of active promoters. Single-nucleosome resolution and high sensitivity allowed us to map tens of thousands of localized spatial interactions between promoters and distal genomic sites. The promoter-centered map of chromatin spatial contacts represents a valuable resource for further research. The quality of the resulting genome-wide profiles is supported by the fact that previously identified spatial contacts, such as contacts of globin gene promoters with their enhancers, are clearly visible.

This study was focused on promoter distant interactions with non-promoter regulatory elements (PIRs). Although P-P interactions were clearly visible in our maps, they were excluded from most of the analyses.

In agreement with previous observations, promoters appear to interact primarily with the surrounding CTCF sites. Interestingly, CTCF-motifs in these sites are typically oriented towards the interacting promoter[52]. This observation can be explained by the putative ability of active promoters to block movement of the loop extrusion complex which can lead to the establishment of promoter-CTCF loops with CTCF motifs preferentially oriented towards the promoters (Fig. 3a, i)[53]. Alternatively, the observed bias might be a consequence of a more general phenomenon known as

architectural stripes, where a CTCF-bound site blocks loop extrusion in a directional manner, causing nonspecific interactions with an extended nearby region[54] (which may include the gene promoter) (Fig. 3a, ii).

Similarly to other MNase-based C-methods, MChIP-C is sensitive enough to identify many relatively weak chromatin interactions that are independent of CTCF binding. The most intriguing group of such spatial contacts is E-P regulatory interactions. We identified 8,472 interactions linking active promoters with distal DHSs bound by a set of enhancer-specific factors. These DHSs are highly enriched with functionally verified K562 regulatory sequences and contain chromatin marks typical for active enhancers (Fig. 3c, Fig. S4a). The proximity between promoters and these enhancer-like DHSs presumably represents the regulatory E-P interactions.

One of the long-standing hypotheses explaining enhancer action at a distance is the E-P looping model[1,2] which assumes that direct physical contact between an enhancer and its target promoter is an essential prerequisite for the promoter activation. Although it is known that at least some enhancers do establish physical contacts with their targets, technical limitations of methods assessing spatial proximity as well as scarcity of functional data on mammalian enhancers prevented accurate systematic evaluation of the E-P looping model. To explain the elusiveness of E-P interactions, it has been suggested that their highly dynamic nature may preclude capturing with existing proximity ligation techniques[55]. Here, we showed that 61.5% of functional enhancer-promoter pairs previously identified in K562 cells using CRISPRi screens[35,36] do establish spatial contacts. Moreover, due to various technical reasons, including insufficient MChIP-C coverage, CRISPRi enhancer mapping mistakes, and indirect regulatory effects, this fraction probably represents an underestimation of the true E-P looping rate. Thus, it is likely that the majority of active enhancers directly interact with target promoters.

Though we have shown that active mammalian enhancers in general interact with the target promoters, we cannot infer this proximity is necessary for target activation. Testing whether it is possible to decouple spatial interactions from gene activity would require understanding the physical nature of these interactions. Various protein factors and a number of physical mechanisms including canonical protein-protein interactions, molecular crowding and liquid-liquid phase separation were implicated in this phenomenon[45,51,56]. One protein complex which was suggested to be involved is cohesin[45,46]. However, in line with studies exploring cellular responses to the acute loss of the cohesin complex[57,58], we observed almost no overlap between regulatory E-P interactions and cohesin binding. Different groups proposed other candidates for the role: the mediator complex, BRD4, YY1 and RNA polymerase II[45,46,50,51,56]. However, recent studies were not able to identify drastic changes in E-P proximity caused by the degradation or the inhibition of any of these proteins[41,58–60]

In order to identify proteins that may be involved in E-P interaction, we assessed the ability of an assortment of ChIP-seq binding profiles to predict the strength of promoter-PIR interaction measured by MChIP-C. As expected, the binding of CTCF and cohesin best predicted the strength of the MChIP-C signal, as the latter is dominated by structural promoter-CTCF interactions. However, we also identified EP300 and SWI/SNF complex as strong predictors of MChIP-C interaction, and they are enriched in enhancer-like PIRs lacking CTCF. These hallmark enhancer proteins were previously shown to bind each other and to share chromatin interaction sites genome-wide[47,48]. Unlike cohesin, mediator, BRD4, YY1 and RNA polymerase II, EP300 and SWI/SNF have rarely been considered as mediators of E-P interaction. However, in our analysis, they consistently outperformed other enhancer-associated factors in terms of predictive power. Although these results may be affected by differences in the quality of the ChIP-seq data, the potential role of EP300 and SWI/SNF in E-P interaction warrants further experimental exploration. Since both EP300 and SWI/SNF are known as chromatin modifiers rather than structural proteins (albeit some studies suggest such a role for EP300[61]), it is possible that their participation in E-P interaction is indirect. To this end, a scenario involving histone acetylation by EP300 may be considered. Although H3K27 residue is a well-

documented EP300 nucleosomal target[62], a recent study identified several other lysine residues localized in H2B N-terminus that are acetylated by EP300[63–65]. These H2B N-terminus acetylation marks correlate with the enhancer activity more strongly than H3K27ac and therefore qualify for being involved in E-P interaction.

Methods

MChIP-C experimental procedure

K562 cells were cultivated in DMEM medium supplemented with 10% fetal bovine serum and 1× penicillin/streptomycin in a humidified 37 °C incubator with 5% CO_2. ~3.5M cells were crosslinked for 10 min at room temperature in 2.5 mL of fresh full growth medium supplemented with 2% formaldehyde (Sigma-Aldrich, F8775). To quench the reaction, glycine was added to reach a final concentration of 0.2 M; the suspension was immediately transferred to ice and incubated there for 5 min. Crosslinked cells were centrifuged at 300g and 4°C, washed with cold phosphate-buffered saline (PBS) and centrifuged again. Pellets were resuspended in 350 µL of cold PBS supplemented with 0.5× protease inhibitor cocktail (PIC) (Bimake, B14001) and 0.5 mM PMSF. Digitonin (Sigma-Aldrich, D-5628) stock solution (1% in DMSO) was added to cells to reach a final concentration of 0.01% A 1 mL tip was used to carefully mix the suspension. Cells were permeabilized on ice for 7 min then centrifuged at 300g and 4°C and resuspended in 800 µL of MNase digestion buffer (10 mM Tris-HCl pH 7.5, 1 mM $CaCl_2$). To achieve a sufficient level of chromatin digestion (50-75% of DNA in mononucleosomal fragments) we added 35-40U of MNase (Thermo Scientific, EN0181) and incubated the cells at 37°C with shaking for 1h. EGTA was added to reach a final concentration of 5 mM in order to stop digestion. Cells were centrifuged at 300g and room temperature, resuspended with a low-retention tip in PBS and transferred to a new, low-retention, tube. We pelleted the material once again at 1000g and resuspended it in 530 µL 1.05× ligation buffer (ThermoScientific, EL0012) supplemented with 0.105 mM dNTPs and 2.1 mM ATP. 50 µL of the material at this stage was separated as a control of digestion efficiency. 100U of T4 Polynucleotide Kinase (NEB, M0201L) and 50U of Klenow fragment of DNA I polymerase (NEB, M0210L) were added to the remaining material in order to repair DNA ends; the mix was incubated at 37 °C with shaking. After 1h 37.5U of T4 DNA ligase (ThermoScientific, EL0012) were added to the reaction and incubation was continued at 37°C for an additional hour. Before leaving the ligation reaction overnight, the mixer was cooled to 20°C and 37.5U more of T4 DNA ligase were added.

The next day, we took 50 µL aliquot as a ligation control, transferred the remaining chromatin to a 2 mL tube and centrifuged it at 5000g. The pellet was resuspended in 550 µL of ice cold ChIP lysis buffer (50 mM Tris-HCl pH 8.0, 1% SDS, 10 mM EDTA) supplemented with 0.5× PIC (Bimake, B14001) and 0.5 mM PMSF. All buffers used in the following sonication and immunoprecipitation steps were precooled to 4°C. We solubilized chromatin with 3 15-sec ultrasound pulses on "15" power setting of VirSonic 100 (VirTis) sonicator. Then, we cleared the solubilized chromatin with 21,000g centrifugation and transferred the supernatant fraction to a 30-kDa Amicon filter (Millipore, UFC503096). We changed the solvent with two successive washes with RIPA buffer (50 mM Tris–HCl pH 8.0, 150 mM NaCl, 1% Triton X-100 (v/v), 0.5% sodium deoxycholate, 0.1% SDS). After the final wash, we transferred the material to a new 1.5 mL tube, brought the volume of RIPA to 1 mL and supplemented it with 1× PIC (Bimake, B14001). Subsequent incubation with antibodies, immunoprecipitation and DNA isolation were performed as previously described[66]. We used 5 µg of polyclonal anti-H3K4me3 antibodies (Active motif, 39016) per MChIP-C experiment. DNA of digestion and ligation controls was isolated in parallel with the immunoprecipitated DNA. After ethanol precipitation, DNA was reconstituted from each sample (controls and the MChIP-C) in 10 µL of 10 mM Tris-HCl buffer (pH 8.0). To assess efficiency of the digestion and ligation, the control samples were run on a 1.5% agarose gel (Fig. S1a).

MChIP-C NGS libraries were prepared from immunoprecipitated DNA with the NEBNext Ultra II DNA Library Prep Kit for Illumina (NEB, E7645) according to the manufacturer's recommendations, with the following modifications: 1) we decreased the reaction volumes two-fold; 2) instead of the adaptor included in the kit, we used 1 μL of barcoded Y-shaped Illumina TruSeq adapters (Illumina, 20015960 and 20015961) per reaction and extended ligation time to 1h. We used 17 μL (~0.37×) of AMPure XP beads (Beckman Coulter, A63881) in the pre-PCR clean-up to select longer DNA fragments and therefore enrich the final library with ligation-informative pairs. Adapter-ligated material was amplified with 12-14 cycles of PCR using KAPA HiFi HotStart PCR Kit (Roche, 07958897001) and universal P5/P7 Illumina primers (see Golov et al., 2019). Post-PCR clean-up was performed without size selection using 1.3× volume of AMPure XP beads (Beckman Coulter, A63881).

Overall, we performed 4 biological replicates of H3K4me3 MChIP-C. The libraries were paired-end sequenced (PE100)on Illumina NovaSeq 6000 and BGI DNBSEQ-T7 devices with ~0.5-1.5B read pairs per library (Fig. S1b, Supplementary Table S2).

H3K4me3 ChIP-seq

~3.5M K562 cells were crosslinked and permeabilized as described above. Permeabilized cells were resuspended in 550 μL of ice cold ChIP lysis buffer (50 mM Tris-HCl pH 8.0, 1% SDS, 10 mM EDTA) supplemented with 0.5× PIC (Bimake, B14001) and 0.5 mM PMSF. Chromatin was sheared with 4 30-sec ultrasound pulses on "15" power setting of VirSonic 100 (VirTis) sonicator. Incubation with antibodies, immunoprecipitation, DNA isolation and NGS library preparation were performed as described MChIP-C protocol, except for the pre-PCR clean-up step where DNA was cleaned with 35 μL (0.76×) of AMPure XP beads (Beckman Coulter, A63881). 12 cycles of PCR were used to amplify ChIP-seq library, and it was paired-end sequenced (PE100) on a Illumina NovaSeq 6000 sequencer with ~6M read pairs. The sequencing reads were aligned to the hg19 genome build and a genome-wide H3K4me3 occupancy profile was generated as described previously[66].

MChIP-C data primary processing

The sequenced reads of each replicate were mapped to the hg19 genome build with BWA-MEM (with -SP5M flags) and parsed with the pairtools package (v.0.3.0). Mononucleosomal (>100 bp and <201 bp apart; convergent) and distal (>5,000 bp apart; cis) read pairs were isolated for downstream analysis.

Mononucleosomal reads were down-sampled to 20M pairs, deduplicated with pairtools and converted to BAM files using samtools (v.1.15.1). Mononucleosomal peaks for each individual replicate were called with MACS2 (v.2.2.7.1) (FDR < 0.0001, maximum gap = 1,000 bp) and 50-bp occupancy profiles were generated with deeptools (v.3.5.1). To compare mononucleosomal profiles of replicates with each other and with conventional H3K4me3 ChIP-seq signal, we calculated read coverage in K562 DHSs (see Supplementary Table S1 for the source of K562 DHS data) for each experiment with deeptools ('multiBigwigSummary BED-file' command), and compared pairwise Pearson correlation coefficients.

We considered genomic regions overlapping mononucleosomal peaks in at least 3 replicates to be consensus peaks. Nearby (< 1,000 bp apart) consensus peaks were merged with bedtools (v2.26.0) resulting in 11,898 MChIP-C viewpoints (Supplementary Table S3). DNase sensitivity, H3K4me3 ChIP and CAGE signals (see Supplementary Table S1 for the source of K562 CAGE data, two CAGE replicates were averaged with bigwigCompare from deeptools) in a 10 kb window centered on each MChIP-C viewpoint and distal DHSs were calculated and plotted with deeptools ('computeMatrix reference-point' & 'plotHeatmap' commands).

Next, we deduplicated distal read pairs using pairtools, produced BAM files and filtered out read pairs that did not map to the identified MChIP-C viewpoints using samtools. Filtered binary files were converted to replicate-specific coverage profiles, or merged MChIP-C profiles, which were then piled

up together into an aggregate merged profile. To analyze and visualize interaction profiles of individual viewpoints, we selected from the merged profile a subset of reads mapping to the viewpoint of interest with samtools ('samtools view -P' command).

To evaluate reproducibility of the distal MChIP-C signal in replicates and to identify promoter-centered interactions, we analyzed the distribution of MChIP-C reads in 250 bp genomic bins. We started with deduplicated distal read pairsam files produced by pairtools; using the data on MChIP-C viewpoints, we extracted positions of distal read pairs mapping to the viewpoints with pairtools ('pairtools split' command) and bedtools ('bedtools pairtobed' command). Each of these read pairs was assigned to a viewpoint; if two reads in a pair mapped to two different viewpoints, the pair was assigned to both viewpoints. Then we overlapped ('bedtools intersect' command) the positions of the mate reads (other-end reads) with 250 bp genomic bins and aggregated the pairs mapping to the same viewpoint and the same other-end bin generating 4 replicate-specific BEDPE files. Each line of the resulting files contained the count of read pairs for a unique viewpoint-genomic bin (other-end bin) pair. To calculate inter-replicate correlation of viewpoint-separated MChIP-C signal, we selected pairs contained within a 1Mb genomic window with only one end mapping inside a viewpoint and estimated inter-replicate Pearson correlation. We also estimated inter-replicate correlation of the merged data. To achieve this, we used merged MChIP-C profiles to create 250 bp-binned coverage dataframes with deeptools ('multiBigwigSummary bins' command), then filtered out bins overlapping viewpoints as well as all bins containing zero reads in at least one replicate and finally calculated inter-replicate Pearson correlation coefficients. To generate distance decay curves, we calculated aggregated MChIP-C signal from replicate-specific BEDPE files in 30 distance bins of equal size on a log10 scale between 3.5 (3,162 bp) and 6.5 (3,162 kbp).

MChIP-C interaction calling

Before merging binned distal MChIP-C signal from all replicates, we normalized it by the replicate-matched mononucleosomal signal. We did this to account for differences of genomic regions in their propensity to be immunoprecipitated with H3K4me3 antibodies. To consider both viewpoint and other-end bin H3K4me3 occupancy, we normalized by mean mononucleosomal coverage of these two regions (we used 'samtools bedcov' command to estimate coverage of each viewpoint and each genomic bin). Next, we summarized all replicate-specific distal MChIP-C signals in each viewpoint-other-end pair.

In order to perform interaction calling, we wanted different viewpoint-specific profiles to be comparable, thus we filtered out pairs separated by more than 2.5 Mb and normalized signal once again, by viewpoint coverage. The viewpoint coverage was defined as a sum of all H3K4me3 occupancy-normalized MChIP-C signal pertaining to the specific viewpoint. The final MChIP-C signal was normalized twice (by H3K4me3 occupancy and by viewpoint coverage), we refer to it as normalized signal.

To reduce noise and avoid calling false positive interactions, we focused on 10,949 viewpoints with raw total coverage (viewpoint coverage before H3K4me3 occupancy normalization in all 4 replicates combined) of more than 1,000 read pairs. To identify viewpoint- other-end pairs with signal significantly exceeding the background, we first assigned each analyzed pair with the distance rank (from 1 for other-end bins directly neighboring the viewpoints to 10,000 for bins separated by 2.5 Mb from the viewpoints). Then, in each distance rank starting with the 20th (since pairs of distal reads were separated by at least 5,000 bp we had almost no signal in the first 19 distance ranks) and ending with the 4,000th, we fitted a Weibull distribution-based background model and called pairs with p-value<0.01 and more than 5 reads (in all 4 replicates together) interactions. We also included pairs with distance rank more than 4,000 and more than 5 reads in MChIP-C interaction list. Finally, we divided all identified interactions into two groups: promoter-promoter (P-P) and promoter-nonpromoter (P-PIR) – depending on whether the other-end bin was localized within a viewpoint (Supplementary Table S4).

Analysis of MChIP-C interactions crossing TAD boundary

We used K562 TAD boundaries from Rao et al.[21]. The expected number of interactions crossing TAD boundaries was defined as a mean count of cross-boundary interactions in 100 independent random permutations changing the positions of the interaction other-ends while preserving the interaction distance distribution. The position of other-end bins in each permutation was established by random reshuffling of distances separating viewpoints from their original interaction partners (bins within other viewpoints or PIRs).

MCC data reanalysis

To estimate the typical proportion of valid ligation pairs in MCC sequencing output, we reanalyzed publicly available datasets from Hua et al.[6] and Downes et al.[67]. We downloaded fastq files for at least 3 biological replicates from each interrogated cell type and mapped them to hg19 or mm10 genomes with bwa (bwa mem -SP5M). Then we parsed reads with pairtools and calculated the fraction of cis-read pairs separated by more than 5,000 bp.

PLAC-seq data reanalysis

To compare MChIP-C data with a similar restriction-endonuclease based C-method, we reanalyzed publicly available H3K4me3 PLAC-seq experiments[37]. Raw sequencing reads were downloaded from the 4D Nucleome Data portal (https://data.4dnucleome.org/experiment-set-replicates/4DNESWX1J3QU/#raw-files) and processed similarly to MChIP-C reads. We relied on MChIP-C-defined viewpoints to obtain merged PLAC-seq profiles and viewpoint-specific PLAC-seq profiles. We used restriction fragment-length bins to build viewpoint-specific PLAC-seq profiles and fixed 250 bp bins to build merged profiles. DNase sensitivity, CTCF ChIP, H3K4me3 ChIP, merged MChIP-C and merged PLAC-seq signals spanning 5 kb regions flanking distal CTCF sites and CTCF-less DHSs were plotted as heatmaps and average profiles with deeptools. Distal CTCF sites with the peak score (the 5th column of CTCF peak file) less than 250 and DHS sites with the signalValue (the 7th column of DHS peak file) less than 200 were excluded from the analysis. In all subsequent analysis concerning DHSs we used the same signalValue cutoff.

Analysis of CTCF motif orientation in viewpoints and PIRs

The presence of CTCF motifs in viewpoints and PIR bins, as well as their orientation, were determined with HOMER (v4.11.1) ("annotatePeaks.pl"). To compare MChIP-C-identified CTCF-based interactions with Hi-C loops, we used the list of 6,057 K562 Hi-C loops identified by Rao et al.[21].

Transcription related factor enrichment analysis in PIRs

To assess transcription-related factor (TRF) enrichment in PIRs we exploited a compendium of publicly available K562 ChIP-seq profiles (see Supplementary Table S1 for a complete list of ChIP-seq datasets used in the present study). The majority of the analyzed datasets were downloaded from the ENCODE portal (268 out of 271). CDK8[68] (CistromeDB: 56379) and MED1 (CistromeDB: 74667) occupancy data were downloaded from the Cistrome database, BRD4[69] – from GEO (GSM2635249). Hg38 datasets were lifted to hg19 with CrossMap (v.0.6.0). All ChIP-seq TRF peaks with the signalValue (the 7th column of each peak file) less than 25 were excluded from all the TRF-related analysis.

First, we overlapped MChIP-C PIRs with TRF binding sites. To estimate relative enrichment, we calculated the expected number of overlaps. We did this for each individual TRF by averaging the overlap counts in 100 independent random permutations, changing the positions of the PIRs while preserving P-PIR distance distribution. The position of PIRs in each permutation was established by random reshuffling of distances separating viewpoints from their original PIRs. Enrichment of TRF binding was then calculated as log2 of the ratio between the experimentally observed and the

expected number of overlaps. Enrichment of TRF motifs in PIRs was evaluated with the HOMER package ("findMotifsGenome.pl" command).

PIR-overlapping DHS clustering and cluster annotation

To separate 18,837 PIR-overlapping DHSs (promoter interacting DHSs) into biologically-relevant groups according to their TRF binding, we used hierarchical clustering with binary features reflecting the binding status of the analyzed TRFs. Here we used only 167 TRFs bound to more than 1,000 promoter interacting DHSs and PIR enrichment higher than 2. We used the Ward's Minimum Variance distance metric for clustering and chose a cutoff of 5 clusters.

For each cluster, we calculated the number of DHSs bound by each of the analyzed TRFs. Next, for each cluster we identified 20 TRFs which were bound to the greatest number of DHSs. Then we merged these 5 sets of TRFs into one list which was comprised of 28 unique TRFs. We plotted the binding of these selected TRFs in PIR-overlapping DHSs as a heatmap (Fig. 3c). To characterize the identified clusters, we overlapped cluster-assigned DHSs with K562 ChromHMM states[70]. We also overlapped DHSs with CRISPRi-verified enhancers from Fulco et al.[35] and Gasperini et al.[36] in order to assess enhancer enrichment of each cluster with a one-sided binomial test.

To calculate the number and distance distributions of MChIP-C interactions associated with the identified DHS clusters, we overlayed the complete set of P-PIR interactions with positions of the promoter-interacting DHSs.

Random forest regression for modeling of MChIP-C signal

We used a random forest regression model (R library "ranger") to predict normalized MChIP-C signal and to identify predictive features. We focused on a subset of viewpoint-DHS pairs separated by <250 kb. We identified 104,166 such viewpoint-DHS pairs with a non-zero count of MChIP-C reads and filtered out 2 outliers (chr16:214,895-215,045 and chr5:693,455-693,605) which were 175 and 82 IQRs above the third quartile. For training the initial model, we used the following features: viewpoint-DHS distance, CTCF motif orientation on both the viewpoint and DHS and CTCF ChIP-seq signal on both the viewpoint and DHS. Training parameters were default with mtry=3, num.trees=100.

Next, we used a greedy forward feature selection approach to add 10 features out of a set of 270 TRF ChIP-seq signals on the DHSs. At each feature selection step, we evaluated all features and added the most predictive feature to the model. To assess the predictive power of a feature, we retrained the model with the feature and used 3-fold cross-validation to evaluate either R^2 or AUC (where MChIP-C was partitioned as higher/lower than the median). To assess reproducibility of the greedy feature selection, we repeated the entire procedure 3 times.

Estimating correlation between chromatin binding of EP300 and SWI/SNF-complex

To compare chromatin binding profiles of histone acetyltransferase EP300 and of the ARID1B, DPF2, SMARCE1 subunits of SWI/SNF-complex in K562 cells, we first calculated ChIP-seq read coverage in K562 DHSs for each of the proteins with deeptools ('multiBigwigSummary BED-file' command). Then we calculated Pearson's correlation between EP300 coverage and coverages of each of the studied SWI/SNF subunits.

Comparing MChIP-C interactions with functionally verified E-P pairs

We used K562 CRISPRi datasets from Fulco et al.[35] and Gasperini et al.[36] to compile a list of 351 verified E-P pairs and 53,660 non-regulatory DHS-P pairs (Supplementary Tables S8 and S9). In order to directly compare these pairs to MChIP-C identified chromatin interactions, we included in this list only pairs with promoters overlapping MChIP-C viewpoints and pairs with distal sites within 5kb-1Mb of the promoter. We extended PIRs of the previously identified MChIP-C interactions by 500 bp in both directions, and overlapped them with E/DHS-P pairs. Using the obtained results, we

separated E/DHS-P pairs in 4 groups: DHS-P pairs lacking MChIP-C interactions (N=50,261), DHS-P pairs with underlying MChIP-C interactions (N=3,399), E-P pairs lacking MChIP-C interactions (N=135) and E-P pairs with underlying MChIP-C interactions (N=216). We excluded all CTCF-bound E/DHS sites and visualized normalized MChIP-C signal around each individual E/DHS site (reflecting proximity between the site and the paired promoter) as a heatmap and the average MChIP-C signals within each of the 4 mentioned groups as an averaged profile.

Data processing and visualization

The following software and packages were used for analysis and visualization: bwa (v.0.7.17), Bowtie2 (v.2.3.4), pairtools (v.0.3.0), samtools (v.1.15.1), bedtools (v2.26.0), deeptools (v.3.5.1), R (v. 4.2.1; dplyr v.1.0.9, tidyr v.1.2.0, ggplot2 v.3.3.6, GenomicRanges v.1.48.0, reshape2 v.1.4.4, fitdistrplus v.1.1-8, RColorBrewer v.1.1-3, dendextend v.1.16.0, dendroextras v.0.2.3, GGally v.2.1.2, ranger v.0.14.1, caret v.6.0-93, PRROC v.1.3.1), HOMER v4.11.1, CrossMap (v.0.6.0), Integrative Genomics Viewer (v.2.8.0), Adobe Illustrator (v.23.0.1).

Author contributions

S.V.R., A.A.G. and A.K.G. conceived and designed the project. A.K.G. performed the experiments. A.K.G. and N.K. analyzed the data and wrote the manuscript draft. All the authors contributed to the interpretation of the results, reviewed, and edited the manuscript and approved the final version.

Acknowledgments

Data availability

MChIP-C and ChIP-seq sequencing data and processed genomic profiles are available at GEO accession GSEXXXXXX.

References

1. Popay, T. M. & Dixon, J. R. Coming full circle: On the origin and evolution of the looping model for enhancer-promoter communication. *J. Biol. Chem.* **298**, 102117 (2022).
2. Ptashne, M. Gene regulation by proteins acting nearby and at a distance. *Nature* **322**, 697–701 (1986).
3. Tolhuis, B., Palstra, R. J., Splinter, E., Grosveld, F. & de Laat, W. Looping and interaction between hypersensitive sites in the active beta-globin locus. *Mol. Cell* **10**, 1453–1465 (2002).
4. Davies, J. O. J. *et al.* Multiplexed analysis of chromosome conformation at vastly improved sensitivity. *Nat. Methods* **13**, 74–80 (2016).
5. Oudelaar, A. M. *et al.* A revised model for promoter competition based on multi-way chromatin interactions at the α-globin locus. *Nat. Commun.* **10**, 5412 (2019).
6. Hua, P. *et al.* Defining genome architecture at base-pair resolution. *Nature* **595**, 125–129 (2021).
7. Montavon, T. *et al.* A regulatory archipelago controls Hox genes transcription in digits. *Cell* **147**, 1132–1145 (2011).
8. Symmons, O. *et al.* The Shh Topological Domain Facilitates the Action of Remote Enhancers by Reducing the Effects of Genomic Distances. *Dev. Cell* **39**, 529–543 (2016).
9. Freire-Pritchett, P. *et al.* Global reorganisation of cis-regulatory units upon lineage commitment

of human embryonic stem cells. *Elife* **6**, (2017).

10. Benabdallah, N. S. *et al.* Decreased Enhancer-Promoter Proximity Accompanying Enhancer Activation. *Mol. Cell* **76**, 473–484.e7 (2019).

11. Karr, J. P., Ferrie, J. J., Tjian, R. & Darzacq, X. The transcription factor activity gradient (TAG) model: contemplating a contact-independent mechanism for enhancer-promoter communication. *Genes Dev.* **36**, 7–16 (2022).

12. Cullen, K. E., Kladde, M. P. & Seyfred, M. A. Interaction between transcription regulatory regions of prolactin chromatin. *Science* **261**, 203–206 (1993).

13. Dekker, J., Rippe, K., Dekker, M. & Kleckner, N. Capturing chromosome conformation. *Science* **295**, 1306–1311 (2002).

14. Denker, A. & de Laat, W. The second decade of 3C technologies: detailed insights into nuclear organization. *Genes Dev.* **30**, 1357–1382 (2016).

15. McCord, R. P., Kaplan, N. & Giorgetti, L. Chromosome Conformation Capture and Beyond: Toward an Integrative View of Chromosome Structure and Function. *Mol. Cell* **77**, 688–708 (2020).

16. Jerkovic, I. & Cavalli, G. Understanding 3D genome organization by multidisciplinary methods. *Nat. Rev. Mol. Cell Biol.* **22**, 511–528 (2021).

17. Lieberman-Aiden, E. *et al.* Comprehensive mapping of long-range interactions reveals folding principles of the human genome. *Science* **326**, 289–293 (2009).

18. Nora, E. P. *et al.* Spatial partitioning of the regulatory landscape of the X-inactivation centre. *Nature* **485**, 381–385 (2012).

19. Sexton, T. *et al.* Three-Dimensional Folding and Functional Organization Principles of the Drosophila Genome. *Cell* **148**, 458–472 (2012).

20. Dixon, J. R. *et al.* Topological domains in mammalian genomes identified by analysis of chromatin interactions. *Nature* **485**, 376–380 (2012).

21. Rao, S. S. P. *et al.* A 3D map of the human genome at kilobase resolution reveals principles of chromatin looping. *Cell* **159**, 1665–1680 (2014).

22. Rowley, M. J. & Corces, V. G. Organizational principles of 3D genome architecture. *Nat. Rev. Genet.* **19**, 789–800 (2018).

23. Hughes, J. R. *et al.* Analysis of hundreds of cis-regulatory landscapes at high resolution in a single, high-throughput experiment. *Nat. Genet.* **46**, 205–212 (2014).

24. Mifsud, B. *et al.* Mapping long-range promoter contacts in human cells with high-resolution capture Hi-C. *Nat. Genet.* **47**, 598–606 (2015).

25. Fullwood, M. J. *et al.* An oestrogen-receptor-alpha-bound human chromatin interactome. *Nature* **462**, 58–64 (2009).

26. Mumbach, M. R. *et al.* HiChIP: efficient and sensitive analysis of protein-directed genome architecture. *Nat. Methods* **13**, 919–922 (2016).

27. Fang, R. *et al.* Mapping of long-range chromatin interactions by proximity ligation-assisted ChIP-seq. *Cell Res.* **26**, 1345–1348 (2016).

28. Gupta, R. M. *et al.* A Genetic Variant Associated with Five Vascular Diseases Is a Distal Regulator of Endothelin-1 Gene Expression. *Cell* **170**, 522–533.e15 (2017).

29. Goel, V. Y. & Hansen, A. S. The macro and micro of chromosome conformation capture. *Wiley Interdiscip. Rev. Dev. Biol.* **10**, e395 (2021).

30. Hsieh, T.-H. S. *et al.* Resolving the 3D Landscape of Transcription-Linked Mammalian Chromatin Folding. *Mol. Cell* **78**, 539–553.e8 (2020).

31. Krietenstein, N. *et al.* Ultrastructural Details of Mammalian Chromosome Architecture. *Mol. Cell* **78**, 554–565.e7 (2020).

32. Canver, M. C. *et al.* BCL11A enhancer dissection by Cas9-mediated in situ saturating mutagenesis. *Nature* **527**, 192–197 (2015).

33. Fulco, C. P. *et al.* Systematic mapping of functional enhancer-promoter connections with

CRISPR interference. *Science* **354**, 769–773 (2016).

34. Gasperini, M., Tome, J. M. & Shendure, J. Towards a comprehensive catalogue of validated and target-linked human enhancers. *Nat. Rev. Genet.* **21**, 292–310 (2020).

35. Fulco, C. P. *et al.* Activity-by-contact model of enhancer-promoter regulation from thousands of CRISPR perturbations. *Nat. Genet.* **51**, 1664–1669 (2019).

36. Gasperini, M. *et al.* A Genome-wide Framework for Mapping Gene Regulation via Cellular Genetic Screens. *Cell* **176**, 377–390.e19 (2019).

37. Chen, P. B. *et al.* Systematic discovery and functional dissection of enhancers needed for cancer cell fitness and proliferation. *Cell Rep.* **41**, 111630 (2022).

38. Lin, X. *et al.* Nested epistasis enhancer networks for robust genome regulation. *Science* **377**, 1077–1085 (2022).

39. Aljahani, A. *et al.* Analysis of sub-kilobase chromatin topology reveals nano-scale regulatory interactions with variable dependence on cohesin and CTCF. *Nat. Commun.* **13**, 1–13 (2022).

40. Goel, V. Y., Huseyin, M. K. & Hansen, A. S. Region Capture Micro-C reveals coalescence of enhancers and promoters into nested microcompartments. *bioRxiv* 2022.07.12.499637 (2022) doi:10.1101/2022.07.12.499637.

41. Ramasamy, S. *et al.* The Mediator complex regulates enhancer-promoter interactions. *bioRxiv* 2022.06.15.496245 (2022) doi:10.1101/2022.06.15.496245.

42. Sanborn, A. L. *et al.* Chromatin extrusion explains key features of loop and domain formation in wild-type and engineered genomes. *Proc. Natl. Acad. Sci. U. S. A.* **112**, E6456–65 (2015).

43. Fudenberg, G. *et al.* Formation of Chromosomal Domains by Loop Extrusion. *Cell Rep.* **15**, 2038–2049 (2016).

44. Rao, S. S. P. *et al.* Cohesin Loss Eliminates All Loop Domains. *Cell* **171**, 305–320.e24 (2017).

45. Kagey, M. H. *et al.* Mediator and cohesin connect gene expression and chromatin architecture. *Nature* **467**, 430–435 (2010).

46. Phillips-Cremins, J. E. *et al.* Architectural Protein Subclasses Shape 3D Organization of Genomes during Lineage Commitment. *Cell* **153**, 1281–1295 (2013).

47. Alver, B. H. *et al.* The SWI/SNF chromatin remodelling complex is required for maintenance of lineage specific enhancers. *Nat. Commun.* **8**, 1–10 (2017).

48. Blümli, S. *et al.* Acute depletion of the ARID1A subunit of SWI/SNF complexes reveals distinct pathways for activation and repression of transcription. *Cell Rep.* **37**, 109943 (2021).

49. Papantonis, A. & Cook, P. R. Fixing the model for transcription: the DNA moves, not the polymerase. *Transcription* **2**, 41–44 (2011).

50. Weintraub, A. S. *et al.* YY1 Is a Structural Regulator of Enhancer-Promoter Loops. *Cell* **171**, 1573–1588.e28 (2017).

51. Hnisz, D., Shrinivas, K., Young, R. A., Chakraborty, A. K. & Sharp, P. A. A Phase Separation Model for Transcriptional Control. *Cell* **169**, 13–23 (2017).

52. Valton, A.-L. *et al.* A cohesin traffic pattern genetically linked to gene regulation. *Nat. Struct. Mol. Biol.* **29**, 1239–1251 (2022).

53. Banigan, E. J. *et al.* Transcription shapes 3D chromatin organization by interacting with loop-extruding cohesin complexes. *bioRxiv* 2022.01.07.475367 (2022) doi:10.1101/2022.01.07.475367.

54. Vian, L. *et al.* The Energetics and Physiological Impact of Cohesin Extrusion. *Cell* **175**, 292–294 (2018).

55. Schoenfelder, S. & Fraser, P. Long-range enhancer-promoter contacts in gene expression control. *Nat. Rev. Genet.* **20**, 437–455 (2019).

56. Papantonis, A. & Cook, P. R. Transcription Factories: Genome Organization and Gene Regulation. *Chem. Rev.* **113**, 8683–8705 (2013).

57. Thiecke, M. J. *et al.* Cohesin-Dependent and -Independent Mechanisms Mediate Chromosomal Contacts between Promoters and Enhancers. *Cell Rep.* **32**, 107929 (2020).

58. Hsieh, T.-H. S. *et al.* Enhancer-promoter interactions and transcription are largely maintained upon acute loss of CTCF, cohesin, WAPL or YY1. *Nat. Genet.* **54**, 1919–1932 (2022).

59. Crump, N. T. *et al.* BET inhibition disrupts transcription but retains enhancer-promoter contact. *Nat. Commun.* **12**, 223 (2021).

60. Zhang, S., Übelmesser, N., Barbieri, M. & Papantonis, A. Enhancer-promoter contact formation requires RNAPII and antagonizes loop extrusion. *bioRxiv* 2022.07.04.498738 (2022) doi:10.1101/2022.07.04.498738.

61. Ma, L. *et al.* Co-condensation between transcription factor and coactivator p300 modulates transcriptional bursting kinetics. *Mol. Cell* **81**, 1682–1697.e7 (2021).

62. Tie, F. *et al.* CBP-mediated acetylation of histone H3 lysine 27 antagonizes Drosophila Polycomb silencing. *Development* **136**, 3131–3141 (2009).

63. Weinert, B. T. *et al.* Time-Resolved Analysis Reveals Rapid Dynamics and Broad Scope of the CBP/p300 Acetylome. *Cell* **174**, 231–244.e12 (2018).

64. Narita, T. *et al.* The logic of native enhancer-promoter compatibility and cell-type-specific gene expression variation. *bioRxiv* 2022.07.18.500456 (2022) doi:10.1101/2022.07.18.500456.

65. Narita, T. *et al.* A unique H2B acetylation signature marks active enhancers and predicts their target genes. *bioRxiv* 2022.07.18.500459 (2022) doi:10.1101/2022.07.18.500459.

66. Golov, A. K., Golova, A. V., Gavrilov, A. A. & Razin, S. V. Sensitivity of cohesin-chromatin association to high-salt treatment corroborates non-topological mode of loop extrusion. *Epigenetics Chromatin* **14**, 36 (2021).

67. Downes, D. J. *et al.* Identification of LZTFL1 as a candidate effector gene at a COVID-19 risk locus. *Nat. Genet.* **53**, 1606–1615 (2021).

68. Pelish, H. E. *et al.* Mediator kinase inhibition further activates super-enhancer-associated genes in AML. *Nature* **526**, 273–276 (2015).

69. Liu, X. *et al.* In Situ Capture of Chromatin Interactions by Biotinylated dCas9. *Cell* **170**, 1028–1043.e19 (2017).

70. Ernst, J. *et al.* Mapping and analysis of chromatin state dynamics in nine human cell types. *Nature* **473**, 43–49 (2011).